Reconfigurable manipulation of perovskite nanoparticles with a cusp-catastrophe Bessel beam

Haixia Wu,[1] Liu Tan,[1] Hui Huang,[1] Xiaofang Lu,[1] Huanpeng Liang,[1] Tao Lin,[1] Bingsuo Zou,[1,2] Peilong Hong,[3,4,*] Yu-Xuan Ren,[5,†] and Yi Liang[1,2,‡]

[1] *Guangxi Key Lab for Relativistic Astrophysics, Center on Nanoenergy Research, Key Laboratory of Blue Energy and Systems Integration, School of Physical Science and Technology, Guangxi University, Nanning, 530004 Guangxi, China*

[2] *State Key Laboratory of Featured Metal Materials and Lifecycle Safety for Composite Structures, Nanning, 530004 Guangxi, China*

[3] *School of Mathematics and Physics, Anqing Normal University, Anqing, 246133 Anhui, China*

[4] *The MOE Key Laboratory of Weak-Light Nonlinear Photonics, TEDA Applied Physics Institute and School of Physics, Nankai University, 300457 Tianjin, China*

[5] *Institute for Translational Brain Research, MOE Frontiers Center for Brain Science, Fudan University, 200032 Shanghai, China*

Exploring reconfigurable axial trapping within perovskite nanoparticles can advance our understanding of their dynamic behaviors, but fine research tools are needed for precise control and modulation. We present a method to study the interaction between perovskite particles and optical fields at the single-particle level, proposing an autofocusing cusp-catastrophe Bessel beam (CCBB) with reconfigurable multiple foci along the propagation direction. The CCBB displays multiple autofocusing with quasi-diffraction-free features. The geometric parameters of the beam can precisely control the quasi-diffraction-free distances, the focus positions, the peak intensities, the trapping forces, etc. Our theoretical proposal for the CCBB has been experimentally corroborated through the generation of the CCBB. We further apply the CCBB to trap $Cs_3Cu_2I_5$ perovskite particles ranging from micrometers to nanometers at multiple longitudinal foci and evaluate the trapping forces at the respective focus. The CCBB offers a potent tool for optical trapping and manipulation, playing a pivotal role in uncovering the interactions between perovskite materials and optical fields.

I. INTRODUCTION

The application of optical trapping and manipulation with novel materials unlocks a multitude of potential possibilities [1–5]. Optical trapping technology gives us the ability to immediately witness nanoscale dynamics, including the interactions between optical fields and particles, as well as the random motion of particles. This insight is critical to understand the behavior of perovskite materials, which cannot be fully captured by static measurements [6,7]. Gaussian beams have traditionally been the primary tool for particle manipulation [8–12], but their inherent properties limit the flexibility of trapping force and positioning. However, recent developments in autofocusing beams [13,14] and nondiffractive beams [15] offer exciting alternatives and have expanded the possibilities for optical manipulation across various fields [16,17].

Abruptly autofocusing fields, characterized by a low-intensity profile in the initial stage and a sudden energy focus [18–20], have attracted widespread attention. For instance, the circular Pearcey beam, which is based on cusp-catastrophe theory, is noted for its enhanced focal contrast, shorter autofocusing length, and the elimination of oscillations after the focus, compared with circular Airy beams [21]. In addition, the diffraction-free beam proposed by Durnin [22] preserves the intensity pattern during propagation in free space. In particular, the circular Bessel beam [23] is renowned for its unique nondiffractive capabilities and excellent self-healing properties [23–25], distinguishing it as a notable example within a broader class of nondiffracting waves. Combining these advantages, we have designed a beam whose propagation characteristics, focusing positions, focal intensities, and potential wells

*Corresponding author: p.l.hong@aqnu.edu.cn
†Corresponding author: yxren@fudan.edu.cn
‡Corresponding author: liangyi@gxu.edu.cn

can be flexibly adjusted, while also reducing photodamage. This adaptability greatly expands the potential applications for optical tweezers across various scenarios.

Here we combine the features of both the circular Pearcey beam and the circular Bessel beam to create an autofocusing cusp-catastrophe Bessel beam (CCBB). Such a combination results in tunable multiple foci and tighter autofocusing effect. The CCBB inherits both the autofocusing property of the Pearcey beam and the nondiffractive property of the Bessel beam. By precisely controlling the spatial offset and the order of the Bessel function, we can reconfigure the CCBB to create multiple foci with variable trapping forces at each focus. This flexibility allows the manipulation of single or multiple $Cs_3Cu_2I_5$ particles at various positions along the propagation direction. Trapping stiffness analysis of these foci further confirms the advantages of the CCBB for optical trapping and manipulation. Our research offers perspectives and possibilities for the use of optical tweezers in the manipulation of perovskite materials.

II. PROPAGATION PROPERTIES OF THE CCBB

The proposed CCBB at the source plane is expressed as

$$\psi(r,0) = A_0 J_a\left(\frac{r_0 - r}{w}\right) V\left(-\frac{r}{w}, 0\right) q(r), \quad (1)$$

where A_0 is the amplitude, the second term represents the finite-energy Bessel beam, and the third term represents the Pearcey beam. J_a is the a th Bessel function of the first kind [24] and $V(t) = \int_{-\infty}^{\infty} \exp\left[i(t^4 + ut^2 + vt)\right] dt$ is the cusp-catastrophe integral [26]. $r = \sqrt{x^2 + y^2}$ is the radial coordinate, where x and y are the transverse coordinates. ω is a transverse scale factor that adjusts the initial intensity distribution. a and r_0 denote the order and spatial offset of the Bessel function, respectively. Specifically, the Heaviside function $q(r)$ takes the value 1 for $r \leq r_1$ and the value 0 for $r > r_1$, defining a region of radius r_1 where the beam is confined.

By use of the input field distribution described by Eq. (1), a comprehensive understanding of the propagation behavior of the CCBB can be achieved through a combination of theoretical analysis, experimental investigation, and numerical simulations using the split-step Fourier method [13,15,27]. This multifaceted approach has been successfully used in previous studies and allows a thorough exploration of the CCBB's properties and its potential applications [28,29].

A. Multi-autofocusing and quasi-non-diffractive propagation

The incident light with a power of 20 mW at a wavelength λ of 532 nm is converted into the CCBB with use of the off-axis hologram [30]. As a demonstration, the CCBB
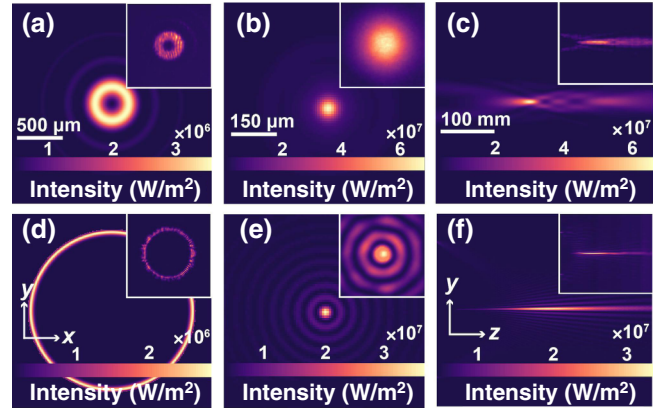

FIG. 1. Theoretical propagation and intensity profiles for (a)–(c) $a = 0$ and (d)–(f) $a = 20$, with the illustrations in the top-right corners showing the experimental results. (a),(d) Results at the source plane $z = 0$ mm. (b),(e) Autofocusing results at $z = f_z$. (c),(f) Side-view propagation, showing the different autofocusing properties of the two beams.

has $\omega = 100$ µm, $r_0 = 2.2$ mm, and $a = 0$ or $a = 20$. A spatial light modulator (Holoeye-LC 2012) loaded with the synthetic off-axis hologram causes the desired wave front to impinge on the incident quasi-plane-Gaussian-beam. Subsequently, the shaped autofocusing CCBB is diagonized with use of a charge-coupled device (DAHENG IMAGING MER-125-30UC) [13].

The cross section of the CCBB with Bessel order $a = 0$, as shown in Fig. 1(a), is characterized by distinct concentric ring structures. Among these rings, the innermost one exhibits the highest intensity. By adjustment of the spatial offset r_0 of the Bessel function, the main ring is shifted outward, which in turn produces a dark spot in the central intensity pattern. As the CCBB propagates to a distance z of 176 mm, it reaches the maximum intensity at the focus, which manifests itself as a bright spot [Fig. 1(b)]. Remarkably, the peak intensity at the focus ($z = 176$ mm) is approximately 10 times larger than the peak intensity at the input plane ($z = 0$ mm), confirming the abrupt autofocusing feature. Beyond the focus, the CCBB undergoes multiple autofocusing oscillations and demonstrates a bottle-shaped region [31], which is highly suitable for the stable trapping of multiple particles, as depicted in Fig. 1(c). The theoretical predictions align closely with the experimental results, validating the accuracy of the theoretical model. Note that the insets in the top-right corners show the experimentally measured beam profiles.

When the Bessel order a increases to 20, the CCBB has a distinctive outer ring with a significant increase in diameter [Fig. 1(d)]. As the CCBB propagates to a distance z of 156 mm, it undergoes automatic focusing, and the intensity of the focused peak is approximately half the intensity
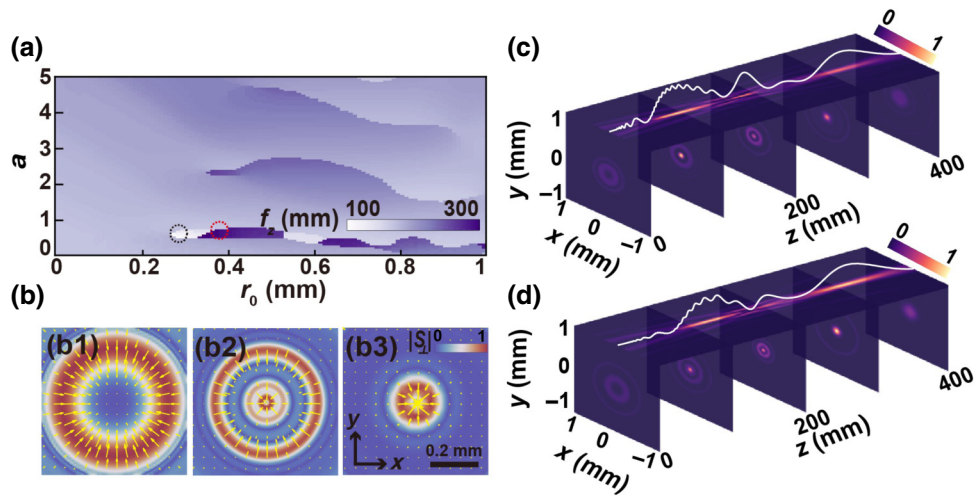
FIG. 2. (a) Autofocusing length f_z of the CCBB with different values of a and r_0. (b) Transverse power flow ($a = 0.6$, $r_0 = 350$ $upmu$ m): (b1) $z = 0$ mm, (b2) $z = f_z$, and (b3) $z = 2f_z$. Side-view and transverse intensity profiles for parameter-value combinations (c) $a = 0.5$ and $r_0 = 280$ μm [labeled with a dashed black circle in (a)] and (d) $a = 0.6$ and $r_0 = 350$ μm [labeled with a dashed red circle in (a)]; the white curves overlaid on the top profile represent the on-axis intensity distribution.

observed with $a = 0$. The focal profile consists of multiple concentric rings [Fig. 1(e)]. Notably, the focus peak not only maintains its intensity level but also continues to propagate without experiencing a rapid drop-off [Fig. 1(f)]. This intriguing behavior is attributed to the increased depth of the optical well during the autofocusing process. Although the CCBB undergoes focusing only once during propagation, the extended depth of the optical well leads to a slower decay of the focus. This phenomenon resembles the nondiffractive-propagation characteristics of a Bessel beam. The observed behavior highlights the potential of the CCBB as a valuable tool for stable, long-range optical communications [32] and optical manipulation [33,34].

B. Tunable multi-autofocusing propagation

The autofocusing behavior of the CCBB can be regulated through the spatial offset r_0 and the order a of the Bessel function. Here we define the autofocusing length f_z as the propagation distance to a focus where the intensity reaches its maximum during propagation. For instance, at $\omega = 100$ μm, the autofocusing length can be regulated by the combination of the mode order a and the spatial offset r_0. As shown in Fig. 2(a), the variation in the focal length represented by f_z for the CCBB is irregular, with most values falling between 175 and 225 mm. The minimum focal length is 93 mm at, $a = 0.5$ and $r_0 = 280$ μm, and the maximum focal length is 318 mm, at $a = 0.6$ and $r_0 = 350$ μm. Video 1 shows how to adjust the separation between the two foci of an CCBB by modifying a and r_0. By changing these parameters, we control the first focus of the CCBB to be approximately 170 mm, while the second focus varies between 200 and 360 mm. As the distance changes, the separation between the two foci decreases

before increasing again. To better illustrate this process and simplify the explanation, we normalize the separation between the two foci to provide a more-straightforward representation of the distance variation.
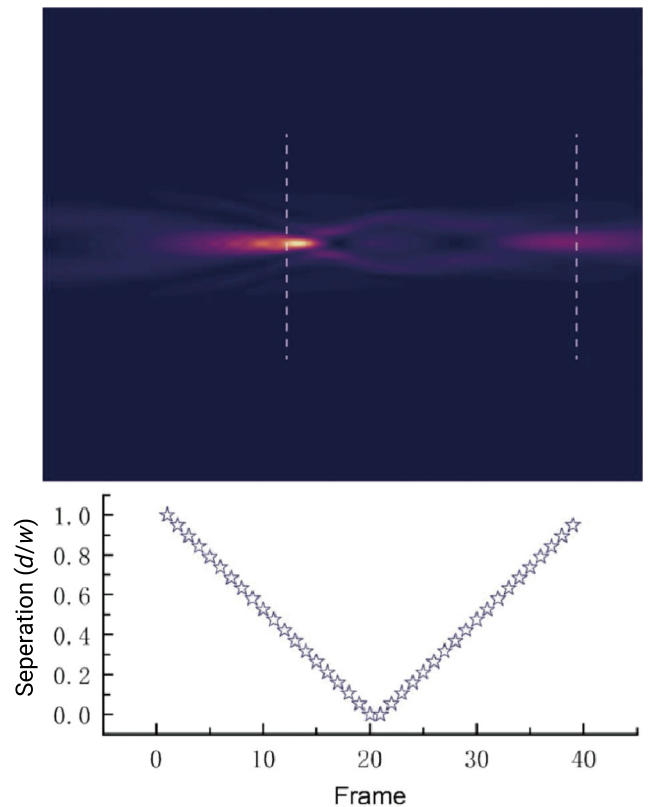
VIDEO 1. The separation between the two foci of the CCBB can be adjusted by variation of the parameters a and r_0.
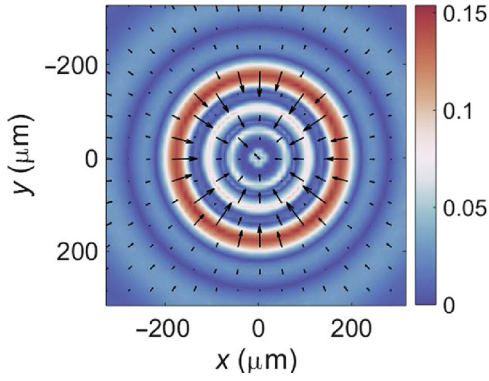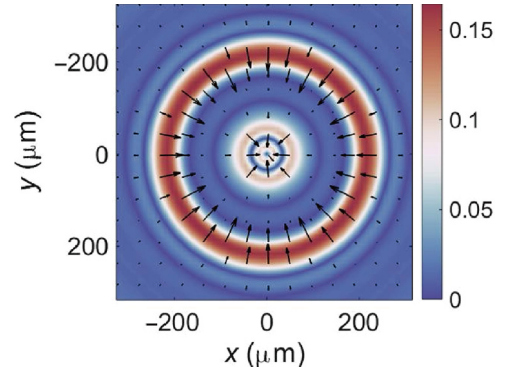
VIDEO 2. Transverse power flow of the CCBB for the parameter-value combination $a = 0.5$ and $r_0 = 280 \, \mu m$.

VIDEO 3. Transverse power flow of the CCBB for the parameter-value combination $a = 0.6$ and $r_0 = 350 \, \mu m$.

To further understand how the beam autofocuses, we analyze the transverse Poynting vector $\vec{S}_\perp$ of the beam. In the paraxial regime, $\vec{S}_\perp$ is given by [35]

$$\vec{S}_\perp = \frac{i}{4\eta_0 k}[\psi \nabla_\perp \psi^* - \psi^* \nabla_\perp \psi], \qquad (2)$$

where $\eta_0 = \sqrt{\mu_0/\varepsilon_0}$ (μ_0 and ε_0 are the permeability and permittivity of a vacuum) is the impedance of free space and $k = 2\pi n/\lambda$ is the wave number of light. Figure 2(b) shows the transverse-power-flow diagrams of the CCBB with the greatest autofocusing length f_z ($a = 0.6$, $r_0 = 350 \, \mu m$) at longitudinal locations $z = 0$, $z = f_z$, and $z = 2f_z$. In the power-flow diagram, yellow arrows represent the direction of the transverse power flow within the CCBB. As the beam propagates, the energy gradually converges toward the center of the beam. The Poynting vector at the center continues to increase until the beam propagates to the first focus. At this focus, there is no net power flow toward the center, resulting in a zero Poynting vector at the most-central position [Figs. 2(b)(b1) and 2(b)(b2)]. Subsequently, the direction of all transverse Poynting vectors near the beam axis shifts from inward to outward. The inflowing power becomes less than the outflowing power, leading to a reduction in the peak intensity and a broadening of the central lobe. This process repeats as the propagation distance increases, resulting in the formation of multiple autofocused foci [as depicted in Fig. 2(b)(b3)]. The power-flow diagram for the shortest autofocusing length f_z ($a = 0.5$, $r_0 = 280 \, \mu m$) exhibits similar characteristics, as described in Sec. 1 in Supplemental Material [36]. Videos 2 and 3 show the variation of transverse power flow in the direction of propagation for the CCBB at the greatest and shortest autofocusing lengths. For clarity and simplicity, the intensity profiles in the simulation are expressed as maximum values, providing a concise representation of the intensity distribution.

To further illustrate the behavior, we select two aforementioned parameters and evaluate the side-view profiles of the beams. We simulate the side-view profiles over a propagation distance of 400 mm and observe multiple autofocusing locations within this range. The top projections represent the propagation side view [Figs. 2(c) and 2(d)]. Specifically, the CCBB exhibits three dominant autofocusing locations, at $z = 93$ mm, $z = 188$ mm, and $z = 315$ mm in sequence, for the parameter values $a = 0.5$ and $r_0 = 280 \, \mu m$ [Fig. 2(c)]. The autofocusing locations can also be regulated to be $z = 125$ mm, $z = 208$ mm, and $z = 318$ mm for the parameter values $a = 0.6$ and $r_0 = 350 \, \mu m$. The maximum intensity occurs at the first focus for Fig. 2(c) and at the third focus for Fig. 2(d). However, because of global modulation $\exp(-\alpha z)$, where α is the absorption coefficient through the perovskite-particle suspension, the first two autofocusing locations always dominate in the light energy. Moreover, our analysis also indicates a progressively increasing depth of the optical well by adjustment of the geometric parameters [Fig. 2(d)].

III. SUPERIOR TRAPPING PERFORMANCE OF THE CCBB

The unique autofocusing properties make the CCBB highly intriguing for the optical trapping and manipulation of particles. The force that traps the Rayleigh particles consists of a gradient force and a scattering force, which are defined as follows [13]:

$$F_g = \frac{1}{4}\varepsilon_0 \varepsilon_m \text{Re}(\alpha) \nabla |\psi^2|, \qquad (3)$$

$$F_s = \frac{1}{6\pi c}\varepsilon_m^3 k_0^4 |\alpha|^2 S, \qquad (4)$$

where ε_0 is the permittivity of a vacuum, ε_p and ε_m are the dielectric permittivities of the particle and the solution, respectively, $\alpha = 4\pi R^3(\varepsilon_p - \varepsilon_m)/(\varepsilon_p + 2\varepsilon_m)$ is the polarizability, R is the radius of the particle, $k_0 = 2\pi/\lambda$ is the wave vector, c is the speed of light in a vacuum, and S is the Poynting vector, respectively. The Rayleigh-scattering theory becomes applicable when the size of the particles
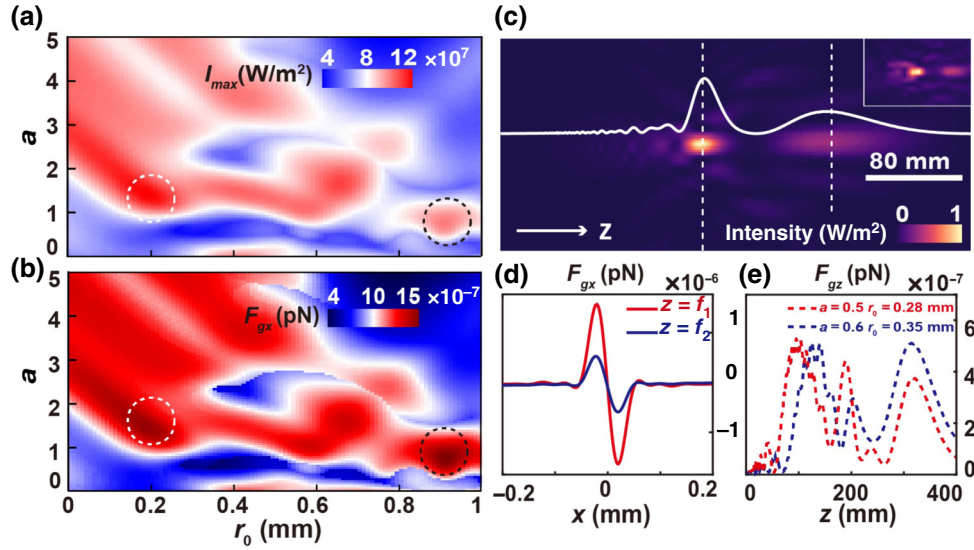
FIG. 3. (a) Maximum focal intensity I_{max} and (b) gradient force F_{gx} of the CCBB as a function of a and r_0. (c) Theoretically simulated side-view propagation ($a = 0.75$, $r_0 = 9.1\,\mu\text{m}$); the inset in the upper-right corner shows the experimental results, and the white curve overlaid in the center represents the axial intensity distribution. (d) Transverse gradient forces at the first and second foci in (c). (e) Longitudinal gradient forces for parameter-value combinations $a = 0.6$ and $r_0 = 350\,\mu\text{m}$ and $a = 0.5$ and $r_0 = 280\,\mu\text{m}$.

is much smaller than the wavelength of the incident light. For polystyrene beads ($R = 50$ nm) as an example, these particles satisfy the Rayleigh approximation when trapped in water ($\varepsilon_p = 2.5$, $\varepsilon_m = 1.7$) and can be treated as simple induced dipoles. In this case, we calculate the gradient force, which is the main force for optical trapping, by applying Rayleigh scattering theory.

In Figs. 3(a) and 3(b), the variation of the gradient force and the light intensity at the focus concerning the parameters a and r_0 is shown. According to Eq. (3), it is evident that the gradient force is directly proportional to the light-intensity gradient, and thus there are certain similarities in the patterns of change between the gradient force and the light intensity, yet anticipated differences also exist. Figure 3(b) illustrates the distribution of the gradient force, which reaches its maximum near the parameter-value combinations $a = 1.45$ and $r_0 = 180\,\mu\text{m}$ (dashed white circle) and $a = 0.75$ and $r_0 = 910\,\mu\text{m}$ (dashed black circle). These parameter-value combinations result in higher gradient forces, indicating stronger trapping capabilities. On the other hand, Fig. 3(a) displays the focal light intensity at different parameter values. It is observed that the focal light intensity at the parameter-value combination $a = 0.75$ and $r_0 = 910\,\mu\text{m}$ (dashed black circle) is lower than at the parameter-value combination $a = 1.45$ and $r_0 = 180\,\mu\text{m}$ (dashed white circle). This indicates that the former configuration results in less light damage, which can be beneficial in applications where minimizing light-induced damage is crucial. The ability to flexibly modulate the gradient force and light intensity at the focus allows optimization

based on specific practical application requirements. By adjustment of a and r_0 of the CCBB, it is possible to tailor the trapping forces and light intensity to achieve optimal performance in various applications.

On the basis of the analysis, we select the parameter-value combination $a = 0.75$ and $r_0 = 910\,\mu\text{m}$ to evaluate the trapping performance of the CCBB. By examining the side view of the propagation and the longitudinal distribution of light intensity in Fig. 3(c), we see that the beam has two foci: one at $z = 177$ mm and the other at $z = 286$ mm. The first focus exhibits 3-times-higher light intensity compared with the second focus. Figure 3(d) displays the transverse gradient forces at the two foci, with the gradient force at the second focus being one third of that at the first focus. As described in Sec. 2 in Supplemental Material [36], the stronger gradient force at the first focus, coupled with its smaller focal spot size, allows more-effective particle trapping and facilitates the observation of particle structure and morphology. The lower light intensity at the second focus implies reduced damage to biological cells, highlighting the potential value of the CCBB in minimizing light-induced damage. Figure 3(e) illustrates the longitudinal gradient forces, with the dotted red line representing the parameter-value combination $a = 0.5$ and $r_0 = 280\,\mu\text{m}$ and the dotted blue line representing the parameter-value combination $a = 0.6$ and $r_0 = 350\,\mu\text{m}$. This observation implies that by adjustment of the parameters of the CCBB, it is possible to control the intensity and position of the traps. Multiple traps can be created, enabling the manipulation of multiple

particles simultaneously. Consequently, the CCBB can be selectively chosen and adapted for different application environments on the basis of specific requirements, such as increasing trapping efficacy or minimizing cell damage.

To experimentally verify the single-particle trapping properties of the CCBB, we built a system of optical tweezers dedicated to the manipulation of individual nanoparticles, capable of accurately monitoring the dynamic information for the perovskite particles [Fig. 4(a)]. Briefly, a spatial light modulator is applied to shape the CCBB, and the autofocusing beam is then directed to an optical microscope through relay optics. The optical trap is formed near the focal plane of an objective lens. The forward-scattering light is further collected by a quadrant photodiode. Specifically, the CCBB is generated at the focal plane of lens 4 and then introduced into the upright microscopy system by a $4f$ imaging system composed of lens 5 and an oil-immersion objective. We chose environmentally friendly lead-free $Cs_3Cu_2I_5$ nanoparticles by a solution-phase method: the cesium oleate precursor solution was first prepared by our placing Cs_2CO_3 (0.305 g), 1-octadecene (15 ml), and oleic acid (0.95 ml) in a 100-ml four-necked flask. Then 1-octadecene (10 ml) and CuI

(0.4 mmol) were put into another 100-ml four-necked flask for high-temperature vacuum drying, 0.5 ml of oleylamine, 0.5 ml of oleic acid, and 4 ml of cesium oleate precursors were injected separately, and the reaction mixture was cooled in an ice-water bath to synthesize $Cs_3Cu_2I_5$ [37]. In the optical trapping experiment, the $Cs_3Cu_2I_5$ perovskite nanoparticles with a radius of about 100–500 nm are dispersed in *n*-hexane. To precisely trap the perovskite particles in a certain autofocusing location, we tune the distance between lens 4 and lens 5 such that the autofocusing position will change concerning the focal plane of the oil-immersion objective lens. Therefore, we can precisely select a particular autofocusing location to trap the perovskite nanoparticles and evaluate the trapping ability for each autofocusing location individually. The power spectrum of the positional signal of a single nanoparticle can be used to evaluate the trap stiffness of the optical trap for each autofocusing location.

We use the first autofocusing point of the CCBB to trap the $Cs_3Cu_2I_5$ perovskite nanoparticles. The beam input power is 20 mW and the parameter values are chosen as $a = 0.75$ and $r_0 = 910$ μm for the CCBB. We use position-sensing detectors (PDQ80A, Thorlabs) to
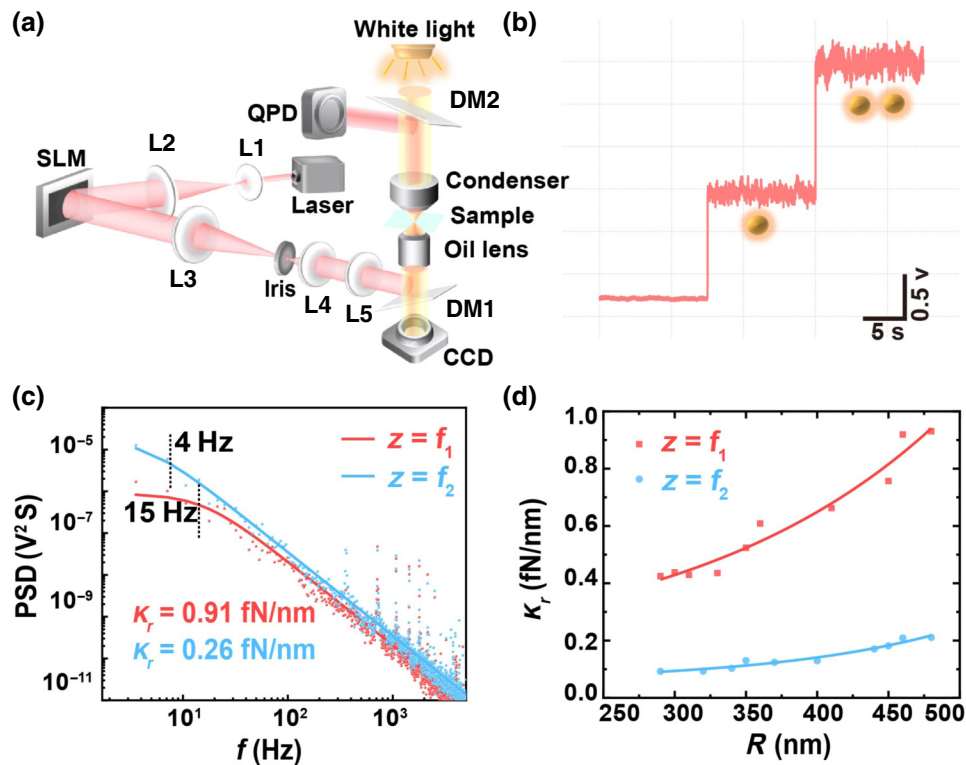

FIG. 4. (a) The structured optical tweezers. (b) Signal-magnitude fluctuation registered on the position-sensing detector suggests the trapping of single and dual perovskite quantum dots of radius 100 nm. (c) Power spectrum of positional signal for a single quantum dot trapped at the first and second foci of the CCBB. The radius R of the $Cs_3Cu_2I_5$ particle is 460 nm and the laser power is 20 mW. (d) Measured trap stiffness increases with the perovskite particle size at the first and second foci of the CCBB. CCD, charge-coupled device; DM1 dichroic mirror 1; DM2 dichroic mirror 2; L1, lens 1; L2, lens 2; L3, lens 3; L4, lens 4; L5, lens 5; PSD, power spectral density; SLM, spatial light modulator.
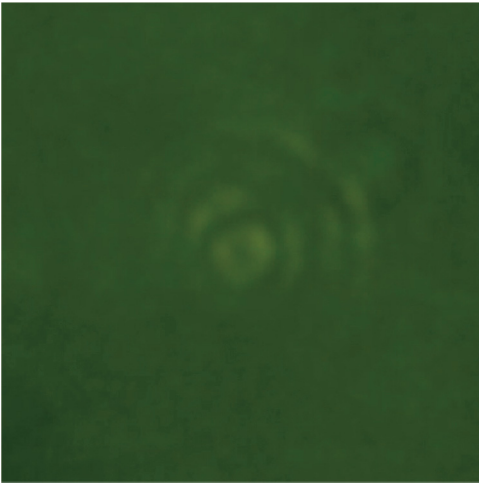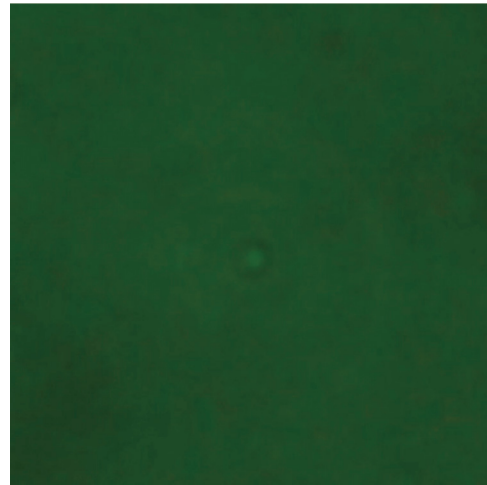
VIDEO 4. Dynamic manipulation of the perovskite particle ($R = 460$ nm) at the first focus of the CCBB.

detect the transverse particle locations and the intensity fluctuation of backscattered light. The backscattered light from multiple particles suggests a different scattering strength as compared with the scattering strength for a single particle, especially when the particle size is below the diffraction-limited resolution of the microscope, i.e., a radius of 100 nm for the nanoparticles used in our experiment. The axial positional signal [Fig. 4(b)] suggests that the trap is empty at the beginning, and when a nanoparticle enters the trap, the signal strength increases immediately. The intensity of the backscattered light continues to increase when more particles enter the same trap. The signal intensity for two particles in the optical trap is higher than that for a single particle. We perform the power-spectrum analysis only on the positional signal for a single particle in the trap, and we find that the corner frequency for the first trap is greater than that for the second autofocusing location [Fig. 4(c)]. The radius of the $Cs_3Cu_2I_5$ particles is 460 nm, and the corner frequency f_c at the first focus of the CCBB (approximately 15 Hz) is greater than that at the second focus (approximately 4 Hz). According to $\kappa_r = 2\pi\gamma f_c$, the trap stiffness at the first focus of the CCBB (approximately 0.91 fN/nm) is about 3 times larger than that at the second focus (approximately 0.26 fN/nm). Thus, the first focus has a greater trapping force ($F_{trap} = \kappa_r \Delta r$) for the same displacement. Videos 4 and 5 show a single perovskite nanoparticle with a radius of 460 nm dynamically trapped at the first and second autofocusing locations of the CCBB, respectively. In experiments, when the radius of the perovskite particles is varied between 280 and 480 nm, the trap stiffness at both foci increases as the particle radius increases [Fig. 4(d)]. In particular, as the particle size becomes comparable to or larger than the wavelength, the scattering force becomes significant and should not be disregarded. In this case, we used the full-wave generalized Lorenz-Mie theory and

Maxwell-stress-tensor technique to calculate the trapping force ($\vec{F}_{trap} = \vec{F}_g + \vec{F}_s$) and stiffness, as detailed in Sec. 3 in Supplemental Material [36]. The trends of the calculated results are consistent with the trends of the experimental results.

To experimentally verify the multiparticle trapping properties of the CCBB, we constructed another system, with a wider field of view, allowing us to observe perovskite particles in both autofocus traps simultaneously [Fig. 5]. An inverted telescope comprising two lenses is used to focus and match the beam size to the particles [Fig. 5(a)]. To visualize the optical beam, we include a small amount of rhodamine 6G in the perovskite suspension dispersed with n-hexane in a cuvette ($10 \times 10 \times 60$ mm^3). The rhodamine 6G solution appears light red and fluoresces in response to the 532-nm excitation, facilitating the observation of the optical path and particle-trapping phenomena. The CCBB is configured with the parameter values $a = 0.75$ and $r_0 = 910$ μm. The cuvette is positioned behind the image focal plane of lens 2 in a $4f$ filter system, with a laser power of approximately 100 mW. To facilitate the capture of particles by the CCBB, we filled the cuvette with a suspension of $Cs_3Cu_2I_5$ particles and then shook it gently. In our experiments, we obtained larger particles through centrifugation, with two distinct median diameters for these $Cs_3Cu_2I_5$ perovskite particles: one at approximately 5 μm and the other at 30 μm.

Figures 5(c) and 5(f) demonstrate the trapping behavior of the CCBB for $Cs_3Cu_2I_5$ particles. When the particle size was 5 μm [Figs. 5(c) and 5(d)], three small stable bright clusters appeared in the cuvette at the first and second foci, as well as between them. Since the trapping force at the first focus is 3 times stronger than that at the second focus, the particles gradually move toward the first focus over time, eventually forming a small bright

VIDEO 5. Dynamic manipulation of the perovskite particle ($R = 460$ nm) at the second focus of the CCBB.
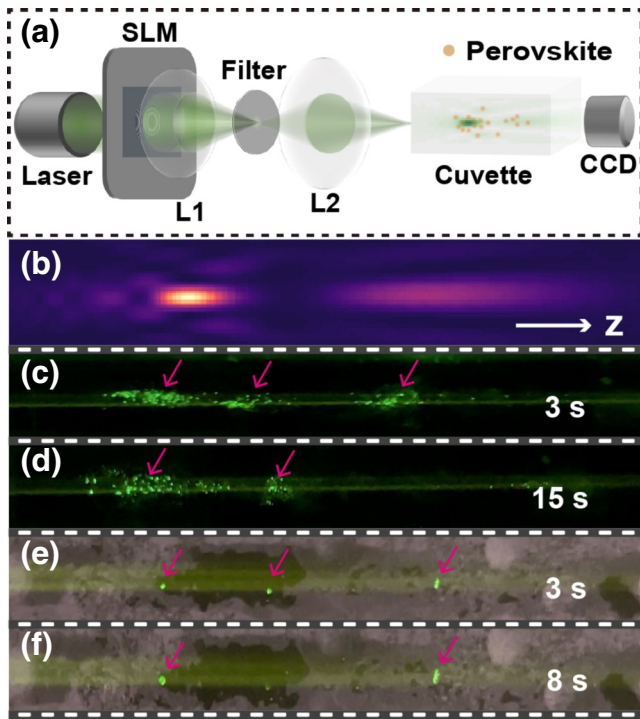
FIG. 5. (a) Experimental setup. (b) Side-view propagation ($a = 0.75$, $r_0 = 9.1$ μm). (c)–(f) Photographs of glass cuvettes taken from the side, where the particle size is (c),(d) approximately 5 μm or (e),(f) approximately 30 μm; the red arrows represent the perovskite particles trapped in the autofocusing location. CCD, charge-coupled device; L1, lens 1; L2, lens 2; SLM, spatial light modulator.

cluster near the first focus. This observation provides evidence that the CCBB has multiple stable trapping points along the direction of propagation, allowing the simultaneous trapping of multiple small particles. When the particle size was increased to 30 μm [Figs. 5(e) and 5(f)], multiple stable bright spots were formed in the cuvette. However, because of the relatively large size of the particles, it becomes challenging to trap a large number of particles simultaneously. This observation confirms that the CCBB possesses multiple stable trapping points along the propagation direction and is capable of stably trapping individual large particles. Videos 6 and 7 show the 1-min
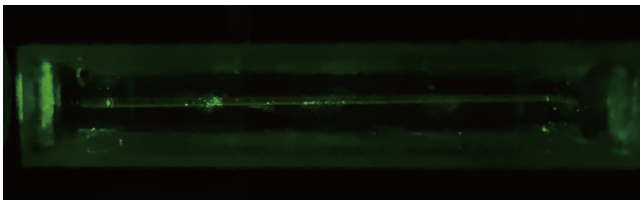
VIDEO 6. Dynamic manipulation of the perovskite particles with $D = 5$ μm.
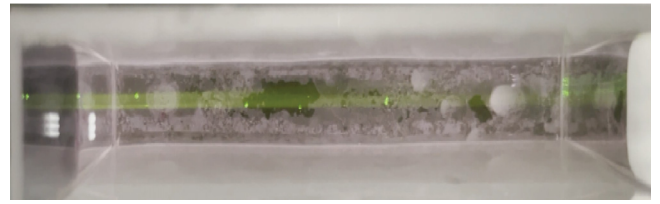
VIDEO 7. Dynamic manipulation of the perovskite particles with $D = 30$ μm.

dynamic trapping and manipulation of the perovskite particles with the CCBB. The CCBB demonstrates its ability to trap particles of various sizes at multiple foci, thereby enabling the manipulation of perovskite particles using optical tweezers.

The first focus in Figs. 5(c) and 5(d) captures more particles than the second. By correlating the scattered-light intensities and the number of particles [as shown in Fig. 4(b)], we determine the number of perovskite particles in the optical trap, thereby making accurate predictions about the clustering behavior of perovskite nanoparticles. This method provides an efficient tool for us to study the clustering properties of perovskite nanoparticles [38,39].

IV. CONCLUSION

In summary, we design a remarkable CCBB with tunable autofocusing and apply the CCBB to the manipulation of perovskite particles of size from tens of nanometers to tens of micrometers. The CCBB combines the strengths of the circular Pearcey beam and the circular Bessel beam, resulting in increased tunability and tighter autofocusing. We demonstrate that perovskite nanoparticles can be faithfully manipulated at each of the autofocusing points under a structured optical tweezer setup. By the tuning of the order and spatial offset of the Bessel function, propagation behavior of the CCBB can be fully reconfigurable, enabling multifocus autofocusing and quasi-diffraction-free propagation. The position of the focus, the peak intensity, and the trapping force can be flexibly controlled as well. The experimental results confirm the presence of multiple stable trapping points along the propagation direction of the CCBB. These trapping points have successfully captured multiple perovskite particles, expanding not only the application of autofocusing beams in the structured manipulation of perovskite particles but also providing a potential research tool for investigating trapping force on particles. Moreover, the proposed CCBB offers excellent performance in terms of propagation properties, autofocusing tunability, and trapping capabilities. It holds promise for various applications that require precise control of light propagation, light intensity, and trapping forces.

ACKNOWLEDGMENTS

---

[1] S.-F. Wang, B. W. Chen, A. Itagaki, F. Ishiwari, T. Fukushima, H. Masuhara, and T. Sugiyama, Manipulation of dual fluorescence behavior in aggregation-induced emission enhancement of a tetraphenylethene-appended polymer by optical tweezers, J. Mater. Chem. C **9**, 7545 (2021).

[2] G. Tkachenko, V. G. Truong, C. L. Esporlas, I. Sanskriti, and S. Nic Chormaic, Evanescent field trapping and propulsion of Janus particles along optical nanofibers, Nat. Commun. **14**, 1691 (2023).

[3] D. Paul, R. Chand, and G. P. Kumar, Optothermal evolution of active colloidal matter in a defocused laser trap, ACS Photonics **9**, 3440 (2022).

[4] K. M. Oliveira, T. A. Moura, J. L. Lucas, A. V. Teixeira, M. S. Rocha, and J. B. Mendes, Use of organic semiconductors as handles for optical tweezers experiments: Trapping and manipulating polyaniline (PANI) microparticles, ACS Appl. Polym. Mater. **5**, 3912 (2023).

[5] L. E. Hillberry and M. G. Raizen, Optically trapped microspheres are high-bandwidth acoustic transducers, Phys. Rev. Appl. **21**, 014031 (2024).

[6] S. A. Kulkarni, S. G. Mhaisalkar, N. Mathews, and P. P. Boix, Perovskite nanoparticles: Synthesis, properties, and novel applications in photovoltaics and LEDs, Small Methods **3**, 1800231 (2019).

[7] S. Wang, A. A. Yousefi Amin, L. Wu, M. Cao, Q. Zhang, and T. Ameri, Perovskite nanocrystals: Synthesis, stability, and optoelectronic applications, Small Struct. **2**, 2000124 (2021).

[8] R. Bresolí-Obach, T. Kudo, B. Louis, Y. C. Chang, I. G. Scheblykin, H. Masuhara, and J. Hofkens, Resonantly enhanced optical trapping of single dye-doped particles at an interface, ACS Photonics **8**, 1832 (2021).

[9] D. G. Grier, A revolution in optical manipulation, Nature **424**, 810 (2003).

[10] A.-I. Bunea and J. Glückstad, Strategies for optical trapping in biological samples: Aiming at microrobotic surgeons, Laser Photon. Rev. **13**, 1800227 (2019).

[11] T. Kudo, B. Louis, H. Sotome, J. K. Chen, S. Ito, H. Miyasaka, H. Masuhara, J. Hofkens, and R. Bresolí-Obach, Gaining control on optical force by the stimulated-emission resonance effect, Chem. Sci. **14**, 10087 (2023).

[12] Y. Liang, G. Liang, Y. Xiang, J. Lamstein, R. Gautam, A. Bezryadina, and Z. Chen, Manipulation and assessment of human red blood cells with tunable "tug-of-war" optical tweezers, Phys. Rev. Appl. **12**, 064060 (2019).

[13] Y. Liang, L. Tan, N. Liu, K. Chen, H. Liang, H. Wu, B. Luo, F. Lu, H. Chen, B. Zou, and P. Hong, Tunable autofocusing and enhanced trapping forces with circular Pearcey Airy beams, Phys. Rev. Appl. **19**, 014016 (2023).

[14] L. Tan, N. Liu, F. Lu, D. Liu, B. Yu, Y. Li, H. Wu, K. Chen, Y. Chu, P. Hong, and Y. Liang, Quantitative characterization of autofocusing and trapping of multi-Airy vortex beams, Phys. Rev. A **107**, 043501 (2023).

[15] T. Moura, U. Andrade, J. Mendes, and M. Rocha, Modulating the trapping and manipulation of semiconductor particles using Bessel beam optical tweezers, Opt. Lasers Eng. **170**, 107778 (2023).

[16] X. Tang, W. Rong, and Y. Shen, Creating optical centrifuge for particle clearing and separation, Opt. Lasers Eng. **167**, 107608 (2023).

[17] C. Wan, Q. Cao, J. Chen, A. Chong, and Q. Zhan, Toroidal vortices of light, Nat. Photonics **16**, 519 (2022).

[18] N. K. Efremidis and D. N. Christodoulides, Abruptly autofocusing waves, Opt. Lett. **35**, 4045 (2010).

[19] M. Manousidaki, D. G. Papazoglou, M. Farsari, and S. Tzortzakis, Abruptly autofocusing beams enable advanced multiscale photo-polymerization, Optica **3**, 525 (2016).

[20] D. G. Papazoglou, N. K. Efremidis, D. N. Christodoulides, and S. Tzortzakis, Observation of abruptly autofocusing waves, Opt. Lett. **36**, 1842 (2011).

[21] X. Chen, D. Deng, J. Zhuang, X. Peng, D. Li, L. Zhang, F. Zhao, X. Yang, H. Liu, and G. Wang, Focusing properties of circle Pearcey beams, Opt. Lett. **43**, 3626 (2018).

[22] J. Durnin, Exact solutions for nondiffracting beams. I. The scalar theory, JOSA A **4**, 651 (1987).

[23] J. Durnin, J. Miceli Jr, and J. H. Eberly, Diffraction-free beams, Phys. Rev. Lett. **58**, 1499 (1987).

[24] D. McGloin and K. Dholakia, Bessel beams: Diffraction in a new light, Contemp. Phys. **46**, 15 (2005).

[25] Z. Bouchal, J. Wagner, and M. Chlup, Self-reconstruction of a distorted nondiffracting beam, Opt. Commun. **151**, 207 (1998).

[26] J. D. Ring, J. Lindberg, A. Mourka, M. Mazilu, K. Dholakia, and M. R. Dennis, Auto-focusing and self-healing of Pearcey beams, Opt. Express **20**, 18955 (2012).

[27] Y. Liang, Y. Hu, D. Song, C. Lou, X. Zhang, Z. Chen, and J. Xu, Image signal transmission with Airy beams, Opt. Lett. **40**, 5686 (2015).

[28] F. Lu, L. Tan, Z. Tan, H. Wu, and Y. Liang, Dynamical power flow and trapping-force properties of two-dimensional Airy-beam superpositions, Phys. Rev. A **104**, 023526 (2021).

[29] F. Lu, H. Wu, Y. Liang, L. Tan, Z. Tan, X. Feng, Y. Hu, Y. Xiang, X. Hu, Z. Chen, and J. Xu, Bessel-modulated autofocusing beams for optimal trapping implementation, Phys. Rev. A **104**, 043524 (2021).

[30] Y. Chen, X. Lin, S. Lin, S. Mo, L. Wan, and Y. Liang, Propagation dynamics of deformed 2D vortex Airy beams, Chin. Opt. Lett. **15**, 080801 (2017).

[31] Y. Wu, Z. Lin, C. Xu, D. Xu, H. Huang, J. Zhao, Z. Mo, J. Jiang, H. Yang, L. Zhang, and H. Liu, Abruptly autofocusing twisted optical bottle beams, Phys. Rev. Appl. **17**, 054014 (2022).

[32] N. Bozinovic, Y. Yue, Y. Ren, M. Tur, P. Kristensen, H. Huang, A. E. Willner, and S. Ramachandran, Terabit-scale orbital angular momentum mode division multiplexing in fibers, Science **340**, 1545 (2013).

[33] K. Dholakia, P. Reece, and M. Gu, Optical micromanipulation, Chem. Soc. Rev. **37**, 42 (2008).

[34] W. Liao, Q. Zhou, Y. Liu, and S. Tao, Segmented-phase high-order Bessel beams, Opt. Commun. **488**, 126849 (2021).

[35] J. Broky, G. A. Siviloglou, A. Dogariu, and D. N. Christodoulides, Self-healing properties of optical Airy beams, Opt. Express **16**, 12880 (2008).

[36] See Supplemental Material at http://link.aps.org/supplemental/10.1103/PhysRevApplied.21.054038 for detailed information on the power flow at the first and second foci of the CCBB, theoretical trapping performance with Rayleigh and non-Rayleigh particles, and animations and videos illustrating the propagation and trapping process of perovskite particles of various sizes.

[37] L. Liao, T. Lin, X. Bin, K. Quan, L. Zhang, R. Zeng, J. Zhai, X. Mo, and J. Zhao, Reabsorption-free luminescent solar concentrator based on environmentally friendly cesium copper halide nanocrystals, J. Lumin. **248**, 118927 (2022).

[38] Y. Jiang, C. Sun, J. Xu, S. Li, M. Cui, X. Fu, Y. Liu, Y. Liu, H. Wan, K. Wei, and T. Zhou, Synthesis-on-substrate of quantum dot solids, Nature **612**, 679 (2022).

[39] E. T. Vickers, Z. Chen, V. Cherrette, T. Smart, P. Zhang, Y. Ping, and J. Z. Zhang, Interplay between perovskite magic-sized clusters and amino lead halide molecular clusters, Research **2021**, 6047971 (2021).